Experimental and theoretical study of the electronic structures of α-PbO and β-PbO_2†

David J. Payne,[a] Russell G. Egdell,*[a] Danny S. L. Law,[b] Per-Anders Glans,[c] Timothy Learmonth,[c] Kevin E. Smith,[c] Jinghua Guo,[d] Aron Walsh[e] and Graeme W. Watson[e]

Received 29th August 2006, Accepted 29th September 2006
First published as an Advance Article on the web 17th October 2006
DOI: 10.1039/b612323f

The electronic structures of α-PbO and β-PbO_2 have been investigated by X-ray photoemission, X-ray absorption and X-ray emission spectroscopies, supported by bandstructure calculations performed within the framework of density functional theory. The relative intensity of a peak found at the bottom of the valence band for both oxides changes dramatically between Al Kα X-ray photoemission and O K shell X-ray emission spectra, demonstrating that the states associated with this peak possess dominant Pb 6s character. This finding is in accord with partial densities of states derived from bandstructure calculations but is at variance with the conventional view that the Pb 6s states in PbO are close to the Fermi energy and hybridise with empty 6p states to give a metal based directional 6s–6p lone pair. The photoemission onset of β-PbO_2 contains a well-defined metallic Fermi edge. The position of the onset structure suggests that the metallic nature of PbO_2 arises from occupation of conduction band states above the main valence band, probably arising from oxygen vacancy defects. The conduction electrons of β-PbO_2 are strongly perturbed by ionisation of Pb core levels, giving rise to distinctive satellites in core XPS whose energies correspond to those of the conduction electron plasmon.

1. Introduction

The heavier post-transition elements such as Tl, Pb and Bi have two important oxidation states: the group state N and the $N - 2$ state. For Pb, the two important oxidation states are II and IV and the simple binary oxides PbO and PbO_2 are prototype Pb(II) and Pb(IV) compounds. The present paper is concerned with electronic structures of the tetragonal polymorphs of these two oxides, α-PbO and β-PbO_2. The Pb cations in α-PbO have a formal $6s^2$ electron configuration and in the simplest ionic picture, oxidation of PbO to PbO_2 involves removal of electron density from the 6s orbital. This viewpoint implies that in β-PbO_2 the 6s band is nominally empty. However, β-PbO_2 is known to be a metallic conductor.[1] It has been argued on the basis of bandstructure calculations that this is an intrinsic property of β-PbO_2 due to overlap between the Pb 6s conduction band and the top of the O 2p valence band.[2] On the other hand the n-type carrier concentration varies markedly with preparative conditions. This suggests that the carriers are introduced by donor defects such as oxygen vacancies or interstitial hydrogen.[3] Technologically, PbO_2 is of ubiquitous importance as the medium for storage of chemical energy on the cathode of lead acid batteries. These batteries have for many years dominated the road transport industry and their manufacture now accounts for over 75% of the usage of lead worldwide. The discharge process involves comproportionation of PbO_2 with spongy Pb metal on the anode in the presence of sulfuric acid to give lead sulfate ($PbSO_4$). Crucial to the ability of lead-acid batteries to deliver the very high currents needed to turn over the starter motor of an internal combustion engine is the fact that PbO_2 is a *metallic* conductor. This ensures that the cathode coating does not contribute significantly to the internal resistance of the battery.[4] Thus it is important to establish *why* this material is metallic.

The crystal structures of $N - 2$ compounds frequently (but not always) involve irregular and non-centrosymmetric coordination environments for the metal cations. α-PbO is typical in this respect.[5] Tetragonal α-PbO (litharge) adopts a structure where four nearest neighbour oxygen atoms form a square on one side of the Pb atoms with four more distant oxygen atoms also in a square arrangement. The long-established conventional explanation of this and related unusual structures is in terms of a metal 6s–6p hybrid "lone pair" orbital which is projected out into the void space within the distorted crystal structure.[6–9] Of course an isolated $6s^2$ cation is spherical. However, the lack of inversion symmetry at the metal sites within a typical distorted $N - 2$ structure allows mixing between occupied metal 6s states close to the Fermi energy (E_F) and nominally unoccupied metal 6p states at higher energy, thus lowering the internal electronic energy of the metal cation and giving a directional s–p hybrid orbital.

[a]*Department of Chemistry, Inorganic Chemistry Laboratory, South Parks Road, Oxford, UK OX1 3QR. E-mail: russell.egdell@chem.ox.ac.uk*
[b]*National Centre for Electron Spectroscopy and Surface Analysis, Daresbury Laboratory, Warrington, Cheshire, UK WA4 4AD*
[c]*Department of Physics, Boston University, 590 Commonwealth Ave., Boston, MA 02215, USA*
[d]*Advanced Light Source, Lawrence Berkeley National Laboratory, Berkeley, CA 94720, USA*
[e]*School of Chemistry, University of Dublin, Trinity College, Dublin 2, Ireland*
† The HTML version of this article has been enhanced with colour images.

Such mixing is not possible at sites that possess inversion symmetry because s and p orbitals have different parity. There is therefore a driving force for structural distortion.

This lone pair model has recently been called into question on the basis of density functional calculations which suggest that the majority of the 6s population in α-PbO is in fact found in a state at the *bottom* of the main valence band, about 10 eV below E_F.[10–12] There is however significant mixing between Pb 6s and O 2p states, giving rise to a filled antibonding state with *some* 6s character at the top of the valence band, but it is not the energy where the majority of the 6s population in the partial density of states is found. Further mixing between the antibonding states and nominally empty Pb 6p states is responsible for the distortion of PbO away from the closely related but higher symmetry CsCl structure. The asymmetric electron density therefore arises predominantly from a mix of O 2p, Pb 6s and Pb 6p orbitals at the top of the valence band, in contrast to the conventional model of a purely metal based 6s–6p lone pair.

In the current paper we present a comprehensive comparative study of the electronic structures of α-PbO and β-PbO_2. High resolution Al-Kα XPS and O K shell X-ray emission are used as complementary probes of the filled valence electronic states whilst empty states are investigated by O K shell X-ray absorption spectroscopy. These experiments provide clear-cut evidence that the maximum in the Pb 6s partial density of states lies well below the Fermi energy in α-PbO and that there is in fact little change in the occupied Pb 6s population between α-PbO and β-PbO_2. These conclusions are supported by density functional theory calculations. The metallic conduction electrons in β-PbO_2 are shown to reside in a band which sits just above the main valence band and gentle annealing in UHV provides a simple means of varying the carrier concentration. The mobile conduction electrons are strongly perturbed in core level photoemission giving rise to distinctive satellite structure. We have investigated the dependence of the core level satellites on both sample pretreatment in UHV and on temperature.

2. Experimental

Phase pure α-PbO was prepared by decomposition of β-PbO_2 at 572 °C.[7] The α-PbO was pelletised between tungsten carbide dies at 2 tons and sintered at 350 °C. Films of β-PbO_2 with the tetragonal rutile structure were deposited on polished Pt substrates by anodic oxidation of solutions of 0.4 M $Pb(NO_3)_2$ in 0.1 M HNO_3. A current density of around 10 mA cm^{-2} and a deposition temperature of 60 °C gave optimal phase purity, with strong reflections in X-ray diffraction (XRD) associated with tetragonal β-PbO_2 and minimal intensity in orthorhombic α-PbO_2 reflections.[13,14] The nominal film thickness was 15 μm. The films were rough but crystalline and displayed pronounced (110) texture. The typical crystallite size as derived from AFM images was about 5 μm (Fig. 1). The films were rinsed in ultrapure water and dried at 100 °C. For comparison a commercial powder sample of phase pure β-PbO_2 was also studied. This was pressed into indium foil. The results from powder and thick film samples were basically identical.

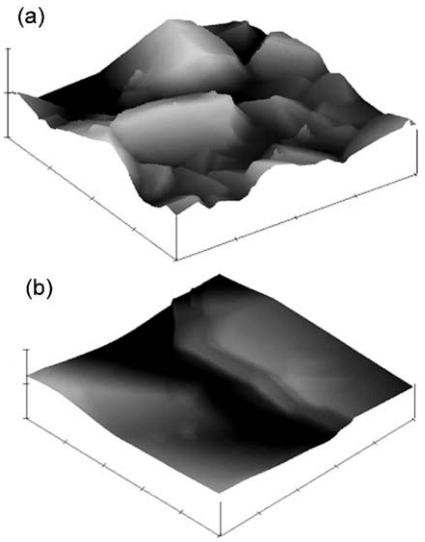

Fig. 1 AFM images of β-PbO_2 films: (a) 20 μm × 20 μm, (b) 5 μm × 5 μm. The height scale range is between 0 and 8 μm in each case.

High-resolution X-ray photoemission spectra (XPS) were measured in a Scienta ESCA 300 spectrometer. This incorporates a rotating anode Al Kα ($h\nu$ = 1486.6 eV) X-ray source, a 7 crystal X-ray monochromator and a 300 mm mean radius spherical sector electron energy analyser with parallel electron detection system. The X-ray source was run with 200 mA emission current and 14 kV anode bias, whilst the analyser operated at 150 eV pass energy with 0.8 mm slits. Gaussian convolution of the analyser resolution with a linewidth of 260 meV for the X-ray source gives an effective instrument resolution of 350 meV. The C 1s to O 1s XPS core level intensity ratio of α-PbO was reduced to below 0.01 by cleaning *in situ* by rear face electron beam heating at 400 °C. Sample charging was problematic and it was necessary to stabilise the surface charge with an electron flood gun delivering 5 eV electrons. Binding energies were referenced to the residual C 1s peak, which was assigned to a binding energy of 284.8 eV by reference to the very weak residual C 1s peak on β-PbO_2. Remarkably, samples of β-PbO_2 were sometimes found to be almost free of carbon contamination even without *in situ* treatments, with a C 1s to O 1s intensity ratio below 1/500. Moreover, core level structure due to the Pt support material was completely absent. The thick film samples of β-PbO_2 were cleaned when necessary by heating at temperatures up to 230 °C. As well as further reducing the level of C contamination, *in situ* heating at this temperatures had a strong influence on the carrier concentration in the films (see below) but the phase integrity as gauged by XRD was not compromised.

X-Ray absorption and emission spectra (XAS and XES) were measured at beamline 7.0.1 at the Advanced Light Source (ALS), Lawrence Berkeley National Laboratory. This beamline is equipped with a spherical grating monochromator.[15] Emission spectra were recorded using a Nordgren-type grazing-incidence spherical grating spectrometer.[16] For resonant emission experiments, the beamline was set to have an energy resolution of 350 meV at the O K edge, and the emission spectrometer was set to have a resolution of 360 meV. Absorption spectra were measured in total electron yield

(TEY) mode by monitoring the sample drain current. The beamline resolution was set to 200 meV for these experiments. The absorption spectra were normalised to a reference current from a clean gold mesh positioned in the path of the photon beam.

3. Computations

For comparison with the experimental data, density functional theory (DFT) as embodied in the Vienna *Ab-initio* Simulation Package (VASP)[17,18] was used to calculate the electronic structure of α-PbO and β-PbO_2. The crystal wave functions were expanded in terms of a plane wave basis set using periodic boundary conditions with a plane wave cutoff of 500 eV and a *k*-point grid density of 6 × 6 × 6 for α-PbO and 4 × 4 × 6 for β-PbO. The generalised gradient approximation (GGA) parameterization of Perdew, Burke and Ernzerhof[19] was used with the projector augmented wave method employed to represent the valence-core interactions[20] (Pb: [Xe]; O: [He]). These fixed core states were generated from all-electron scalar relativistic calculations. The metal 5d states were included explicitly in the calculations, but the extent of hybridization of these states with O 2p states was negligible. In contrast to previous *ab initio* studies,[21] full optimization of the crystal structures was performed.

Structural optimizations at a series of volumes were performed, allowing the atomic positions, the lattice vectors and angles to relax within a constrained total volume. The resulting energy *versus* volume curve was fitted to the Murnaghan equation of state[22] to obtain the equilibrium cell volume. This approach avoids the problems in Pulay stress associated with volume changes within a plane wave basis set. The optimized crystal structures of both α-PbO and β-PbO_2 are shown in Fig. 2. The calculated lattice vectors of α-PbO were $a = b = 4.06$ Å and $c = 5.39$ Å. These are within 2.5% of experiment with the exception of the *c* vector which is overestimated by 7.8%. This reflects the inability of density functional methods to model the weak van der Waals forces between PbO layers in the *c* direction. However the optimized Pb–O bondlength is within 1.3% of the experimental value, showing an accurate description of bonding within the Pb–O layers. The error in the Pb–O bondlength is similar to a value of 1.2% found in a recent calculation on *molecular* PbO using a hybrid DFT/Hartree–Fock Hamiltonian.[23] The calculated lattice parameters for β-PbO_2 were $a = b = 5.08$ Å and $c = 3.45$ Å, representing small deviations of only +2.5% and +2.0% respectively from experimental values.

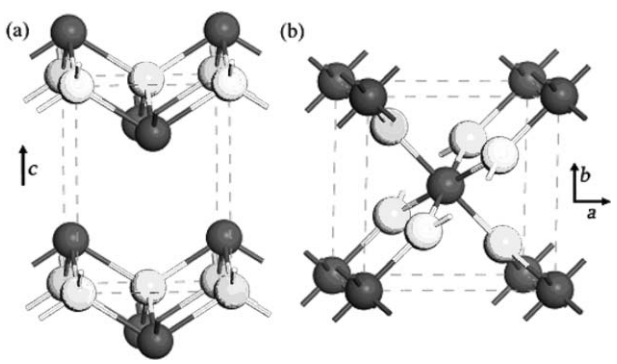

Fig. 2 The optimized crystal structures of (a) α-PbO and (b) β-PbO_2. The Pb atoms are coloured dark grey, with oxygen light grey.

4. Results and discussion

4.1. The calculated densities of states

The calculated total and partial densities of states for α-PbO are shown in Fig. 3. Within the occupied density of states it is possible to identify three main features labelled I–III in the figure. Integration across the occupied states reveals that III corresponds to two electron states per formula unit, whilst I and II contribute six electron states per formula unit. All three have pronounced O 2p character but the states associated with the peak III, which is found at the highest binding energy, actually has dominant Pb 6s character and is derived from an in phase bonding combination with O 2p states. The middle

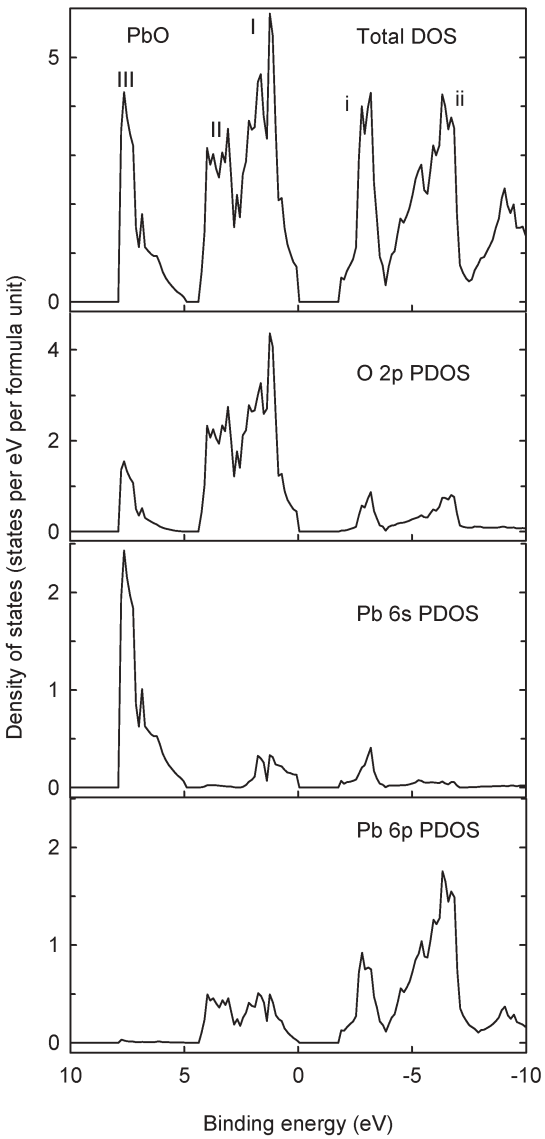

Fig. 3 The total and partial densities of states for tetragonal α-PbO. The Pb 6s and Pb 6p partial densities of states are presented on a scale expanded by a factor of 2 relative to the other data.

peak II has very little Pb 6s character, but there is significant admixture of Pb 6p states into the states in the middle of the valence band. The highest valence band states responsible for peak I also have a significant contribution from Pb 6p states together with a smaller contribution from Pb 6s states which combine out of phase with O 2p states to give an antibonding state. The overall pattern of electronic structure is very similar to that found in molecular PbO where the topmost 4σ MO is found to involve significant Pb–O antibonding character as well as directional Pb lone pair character.[23] The empty density of states has two main peaks within 10 eV of the Fermi energy, labelled i and ii in Fig. 3. The lower of these, i, has some Pb 6s and O 2p character together with a bigger contribution from Pb 6p states. The higher peak, ii, contains little Pb 6s character and is essentially a mix of Pb 6p and O 2p states. The bandgap derived from our calculations has a value of 1.7 eV, compared with an empirical value of 1.95 eV at room temperature.[24–26] It is generally recognised that density functional methods tend to underestimate bandgaps,[27] although the discrepancy in this case is quite small.

The corresponding density of states profiles for β-PbO_2 are shown in Fig. 4. Again it is possible to identify three main features labelled I–III in the occupied density of states and two features i and ii in the empty density of states. I–III now account for twelve electron states per formula unit, but with III again contributing two states. As with α-PbO, the states in band III contains a mix of Pb 6s and O 2p character. There is

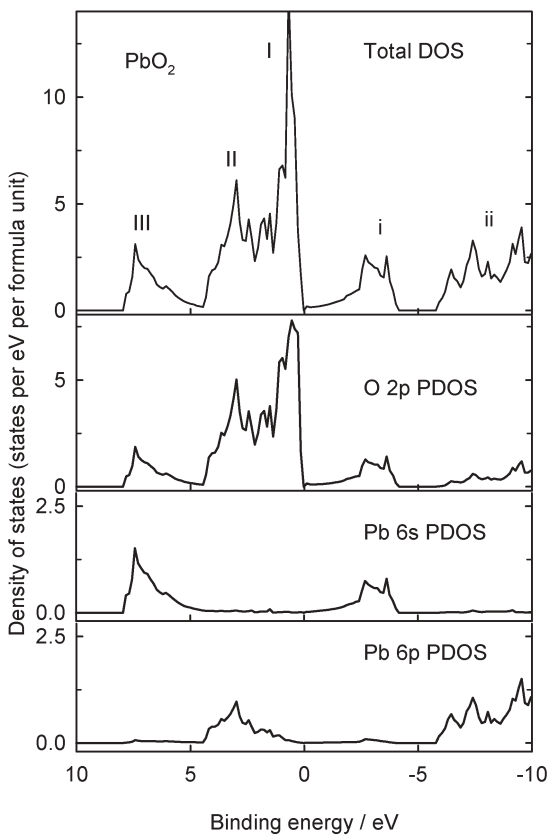

Fig. 4 The total and partial densities of states for tetragonal β-PbO_2. The Pb 6s and Pb 6p partial densities of states are presented on a scale expanded by a factor of 2 relative to the other data.

now little Pb 6s or Pb 6p character in the states in band I at the top of the valence band. Instead the 6s character is split between the occupied states in band III discussed above and the empty states in band i. Similarly the Pb 6p character is split between the occupied states in band II and the empty states in ii. There is thus very little direct hybridisation between Pb 6s and Pb 6p states in either the occupied or the empty states. In particular there is clear separation between the Pb 6s and Pb 6p conduction band states, with a region between 4.2 eV and 5.8 eV above the Fermi energy where the density of states drops to zero. Another important distinction between α-PbO and β-PbO_2 is that the bandgap is very much bigger in the former. The top of the valence band and the bottom of the conduction band do not overlap for β-PbO_2 and the density of states does drop to zero at E_f, but in our calculations the full and empty bands almost touch. Recognising that density functional methods inevitably underestimate bandgaps, we may infer that β-PbO_2 has a small but non-zero bandgap.

In summary α-PbO and β-PbO_2 are both found to be highly covalent materials with very strong hybridisation between O 2p and Pb 6s and 6p states. Bader partitioning[28] of the charge density on the Pb cations gives a value of only +2.1*e* to Pb in β-PbO_2 and +1.2*e* to Pb in α-PbO. These values are roughly half the formal ionic charge. Moreover, the effective Pb 6s population per Pb ion derived by integrating the Pb 6s partial density of states (PDOS) is 1.0 in β-PbO_2, as compared with 1.4 in α-PbO which is formally a $6s^2$ compound.

4.2. Valence XPS and O K shell XES

Valence band XPS spectra of α-PbO and β-PbO_2 are shown in the top left panels of Fig. 5 and 6 respectively alongside calculated total densities of states derived from the DFT calculations. The XPS spectra for both α-PbO and β-PbO_2 are in general agreement with previously published data.[26,29–31] For each oxide it is again convenient to discuss the structure of the valence band in terms of three features, labelled I, II and III. For α-PbO the low binding energy peak I apparently consists of two overlapping components with indication of a high binding energy shoulder. Peak II appears as a well-defined high binding energy shoulder to I, while peak III, which appears at the highest binding energy of 9.8 eV, is well-resolved from the rest of the valence band and shows signs of a low binding energy shoulder. Three spectral features are also found for β-PbO_2, although peak III is now weaker relative to I and II than for α-PbO. In broad terms the X-ray photoelectron spectra reproduce the total density of states derived from the bandstructure calculations. The major discrepancy is that the overall energy spread of valence band states is less in the calculations than is found experimentally. This is a general problem when comparing densities of states (DOS) derived from DFT calculations with experimental photoemission spectra.[27] The fact that for α-PbO and β-PbO_2 XPS appears to measure the total DOS suggests that cross sections for ionisation of O 2p, Pb 6s and Pb 6p states are all very similar. Within the framework of the Gelius model,[32] this conclusion is not in accord with the widely used ionisation cross sections of Yeh and Lindau, where the Pb 6p and 6s one electron ionisation cross sections are calculated to be much

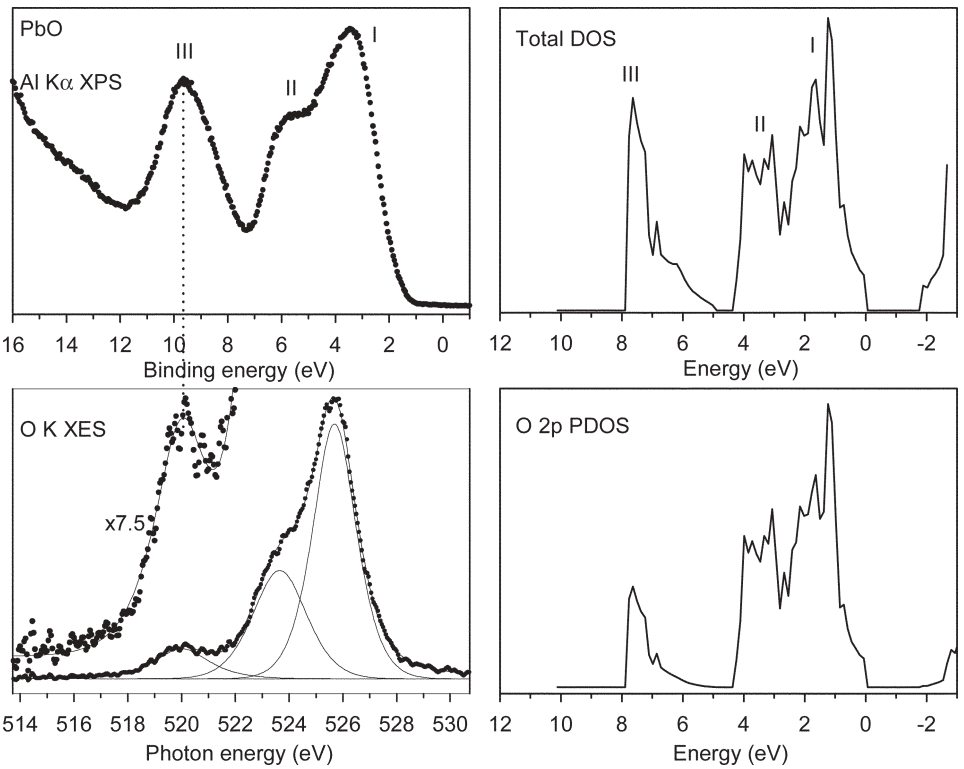

Fig. 5 Valence band Al Kα XPS and O K shell XES spectra from α-PbO compared with the total DOS and the O 2p PDOS derived from DFT bandstructure calculations. The alignment between the XPS and XES spectra is made on peak III. Note that the overall spread of energies is 17 eV in the experimental spectra but only 15 eV in the calculated DOS.

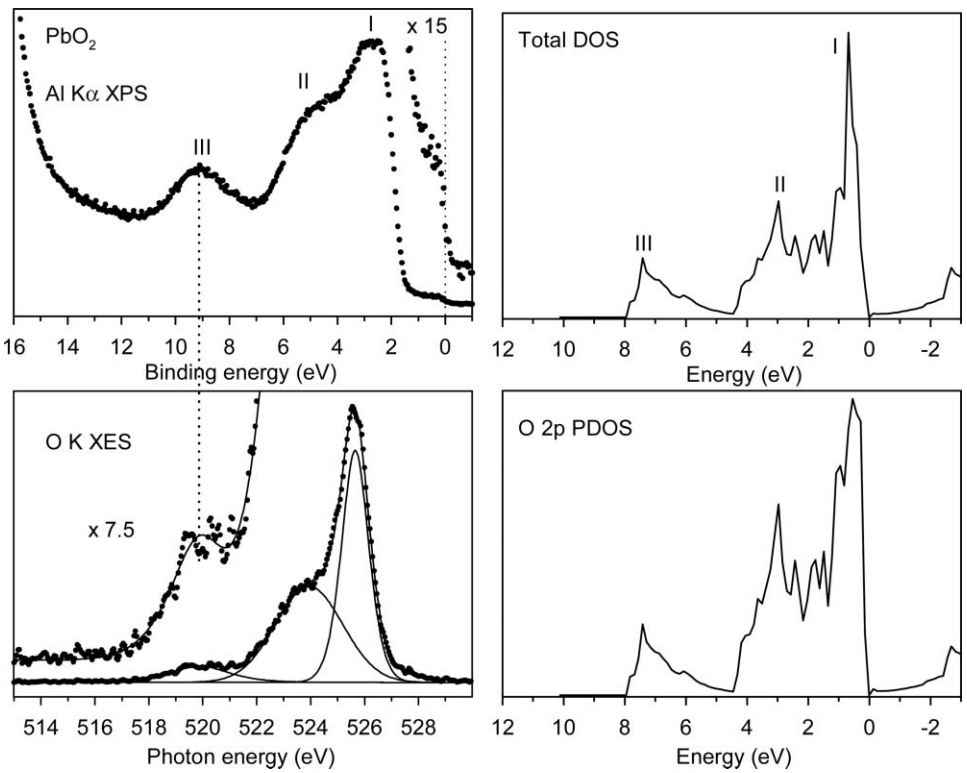

Fig. 6 Valence band Al Kα XPS and O K shell XES spectra from β-PbO_2 compared with the total DOS and the O 2p PDOS derived from DFT bandstructure calculations. The alignment between the XPS and XES spectra is made on peak III. Note that the overall spread of energies is 17 eV in the experimental spectra but only 15 eV in the calculated DOS.

larger than the O 2p cross section.[33] The discrepancy cannot be simply attributed to relativistic effects not treated in these cross section calculations because the Pb 6s and Pb 6p cross sections calculated by Scofield[34] using a relativistic Dirac–Slater method are very similar to those of Yeh and Lindau. Thus cross section weighted densities of states calculated using the tabulated cross sections give too much intensity to bands II and III relative to I. The uncertainty in cross sections highlights a difficulty in using XPS data alone as a source for derivation of information about partial densities of states (PDOS).

A final feature of the XPS of β-PbO_2 is that the spectra terminate in a weak but well defined Fermi edge which straddles zero binding energy. Analysis of this structure and its variation with *in situ* annealing treatment is discussed further below.

O K shell emission spectra of the two oxides are shown in the lower left hand panels of Fig. 5 and 6. Again it is possible to identify three bands. There are however very pronounced changes in relative intensities as compared with the XPS data. Most strikingly the high binding energy band III is very much weaker relative to I and II in XES as compared with XPS. Due to the localised nature of the O 1s core hole and the dipole selection rule operative in X-ray emission, the O K shell emission spectra involve decay from occupied states of O 2p character into an O 1s core hole. O K emission therefore directly measures the O 2p PDOS. Thus the diminution of intensity of band III is a clear signature of the fact that the corresponding electronic states at the bottom of the valence band have less O 2p character than the states closer to E_F. The reduced contribution of the O 2p levels to the PDOS in band III is also seen clearly in the calculations.

To quantify this idea, it is possible to make an estimate of the O 2p contribution f_{O2p} to the lowest valence band state from the XES data as follows. Integration of the calculated density of states across band III reveals that it corresponds to two electron states per metal atom for both PbO and PbO_2. If *all* the states in the valence band were of pure O 2p character it follows that the intensity of band III (I_{III}) relative to that of the total valence band (I_{total}) would simply be n/p where n is the number of metal atoms per formula unit and p is the total number of valence electron pairs per formula unit ($n = 1$, $p = 4$ for PbO; $n = 1$, $p = 6$ for PbO_2) It follows that the fractional contribution of O 2p states to the lowest valence band f_{O2p} may be estimated from the ratio between the intensity I_{III} of the lowest valence band peak measured in XES and the total experimental valence band intensity I_{total}.

$$f_{O2p} = \frac{(I_{III}/I_{total})}{(n/p)}$$

The results of this analysis for PbO and PbO_2 are given in Table 1, along with data for HgO, Tl_2O_3 and Bi_2O_3.[35–38] Corresponding values obtained by integrating the partial density of states from the DFT calculations are also given. Both the experimental and calculated data clearly show that there is a progressive decrease in the amount of O 2p character in the valence band state at highest binding energy in moving across the periodic table. For both the lead oxides there is in fact less than 50% O 2p character present in the lowest valence band state. Empirically we can therefore deduce that the state at the bottom of the valence band must have dominant metal 6s atomic character and that the amount of 6s character present is not much different between the two oxides.

Table 1 Estimates of O 2p contribution to lowest valence band state from XES data and from DFT bandstructure calculations

	XES	DFT
HgO	0.87	0.82
Tl_2O_3	0.54	0.47
PbO_2	0.43	0.28
PbO	0.37	0.30
Bi_2O_3	0.19	0.17

The empirical values in Table 1 assume that the states in bands I and II are of pure O 2p atomic character. There is in fact some mixing of 6s and 6p character into these states, although Fig. 3 and 4 show that the extent of the mixing is quite small. Nonetheless, due to this mixing the experimental values given in Table 1 must overestimate the true amount of O 2p character in the lowest valence band state. This accounts for the small systematic discrepancy between experimental and theoretical values.

4.3. O K shell XAS and resonant XES

The O K shell X-ray absorption spectrum of α-PbO is shown in the upper panel of Fig. 7. There are two peaks labelled i and ii above the threshold with a separation of 2.8 eV between the maxima. Peak i is narrower than ii and has a symmetric lineshape. By contrast ii has a well-defined high energy shoulder. In broad terms this structure is reproduced in the calculated O 2p partial density of states (Fig. 3) where there are also two peaks, but with a separation of 3.3 eV. The lower peak corresponds to O 2p states hybridised with both Pb 6s and 6p states, whereas the higher peak is associated with O 2p states hybridised only Pb 6p states.

The O K shell X-ray absorption spectrum of β-PbO_2 is shown in the upper panel of Fig. 8. Again it possible to identify two main peaks i and ii, but in this case the second peak ii clearly consists of three overlapping components, the second of which gives the maximum in the overall band profile. The separation between the maxima of i and ii is 7.05 eV. Again the experimental spectrum parallels the structure found in the O 2p partial density of states where the separation between a lower band of O 2p states hybridised with Pb 6s states and an upper band where the O 2p states are hybridised with Pb 6p states is bigger than for α-PbO.

4.4. Core level XPS

Pb 4f core level spectra of α-PbO and β-PbO_2 in the Pb 4f region are shown in Fig. 9. The 4f spectrum of α-PbO comprises a simple spin–orbit doublet with a spin–orbit splitting of 4.86 eV. The individual components have a full width at half maximum height of 0.93 eV. The core lineshape for β-PbO_2 is more complex. The individual spin–orbit components display an asymmetric peakshape which can be fitted with two pseudo-Voigt components separated by 0.69 eV.

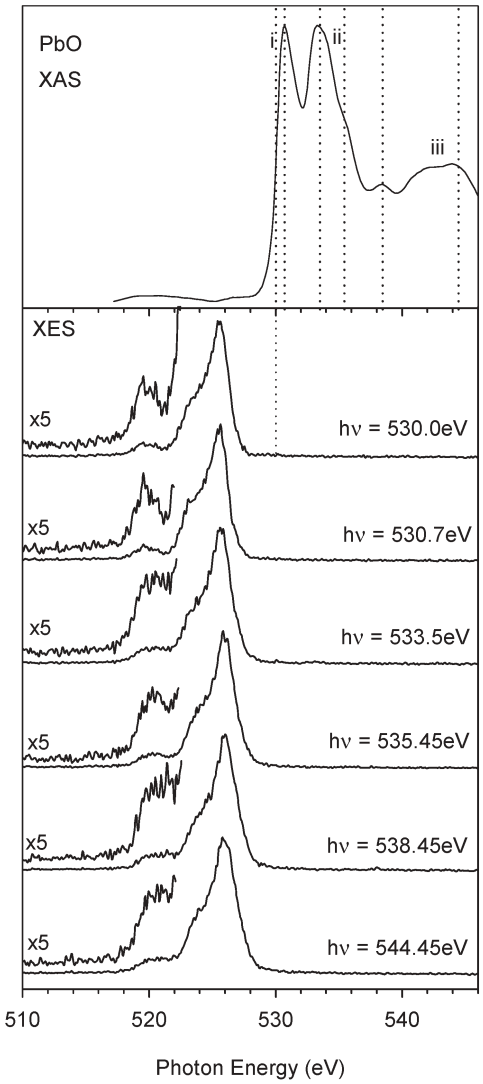

Fig. 7 Upper panel: X-ray absorption spectrum of α-PbO in the region of the O 1s core threshold. The vertical dashed lines delineate photon energies at which emission spectra have been excited in the data presented below. Lower panel: X-ray emission spectra of α-PbO excited at the photon energies indicated. The threshold photon energy is indicated by a vertical dashed line.

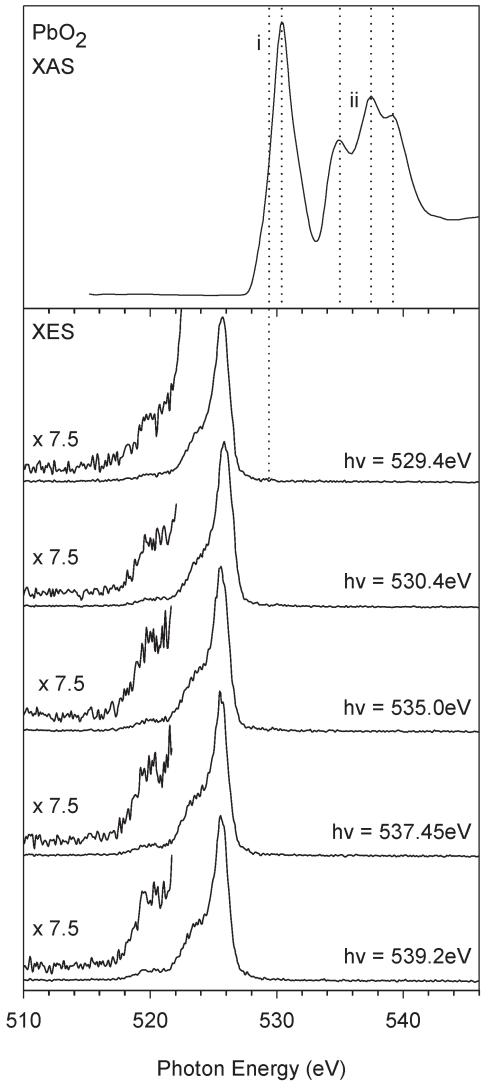

Fig. 8 Upper panel: X-ray absorption spectrum of β-PbO_2 in the region of the O 1s core threshold. The vertical dashed lines delineate photon energies at which emission spectra have been excited in the data presented below. Lower panel: X-ray emission spectra of β-PbO_2 excited at the photon energies indicated. The threshold photon energy is indicated by a vertical dashed line.

The lower components are sharper (FWHM = 0.67 ± 0.1 eV) than the higher binding energy "satellites" (FWHM = 1.34 ± 0.1 eV). It is also striking that the high binding energy components are more pronouncedly Lorentzian than the low binding energy components suggesting that the linewidth of the former is dominated by lifetime broadening. Similar but weaker satellite structure is found on the O 1s core line of β-PbO_2 where the separation between the two components is again close to 0.69 eV (a value of 0.72 eV is obtained from the curve fit of Fig. 10). By contrast the O 1s spectrum of α-PbO fits to a simple Voigt function. A weak component shifted by a much larger energy of 2.06 eV from the main peak arises from residual surface contamination by hydroxide or carbonate species.

The core photoemission spectra of β-PbO_2 are very similar to those of other metallic post transition metal oxides including Sb-doped SnO_2,[39,40] Sn-doped In_2O_3,[41] and Tl_2O_3.[36] The observation of strong intrinsic satellites for PbO_2 but not for PbO is obviously a direct consequence of the metallic nature of the former. The simplest model is that the broad high energy peaks correspond to unusually strong conduction electron plasmon satellites. The plasmon energy is determined by the carrier concentration n through the relationship:

$$\omega_p^2 = \frac{ne^2}{m^*\varepsilon_0\varepsilon(\infty)}$$

where ω_p is the plasmon frequency, m^* is the effective mass and $\varepsilon(\infty)$ the high frequency dielectric constant. The separation of the "satellite" from the main peak, 0.69 eV, is in fact very similar to the plasmon energy of 0.76 eV measured directly by electron energy loss spectroscopy.[42]

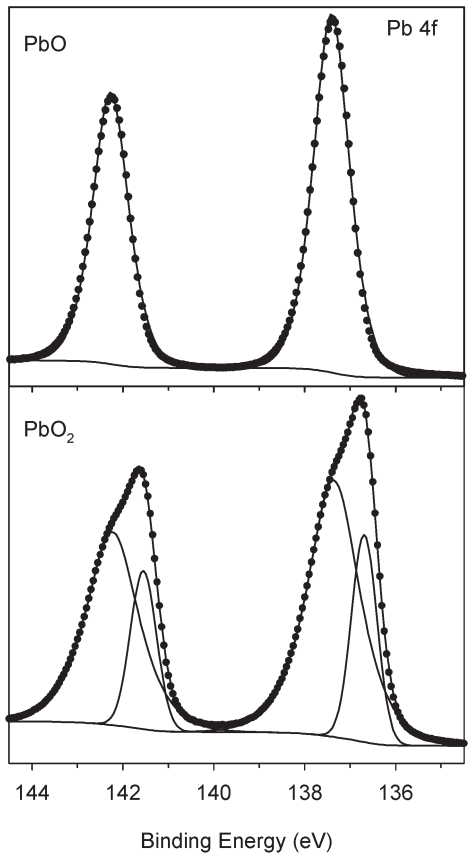

Fig. 9 Al Kα core level photoemission spectra of α-PbO and β-PbO_2 in the Pb 4f region. See text for discussion of energy referencing.

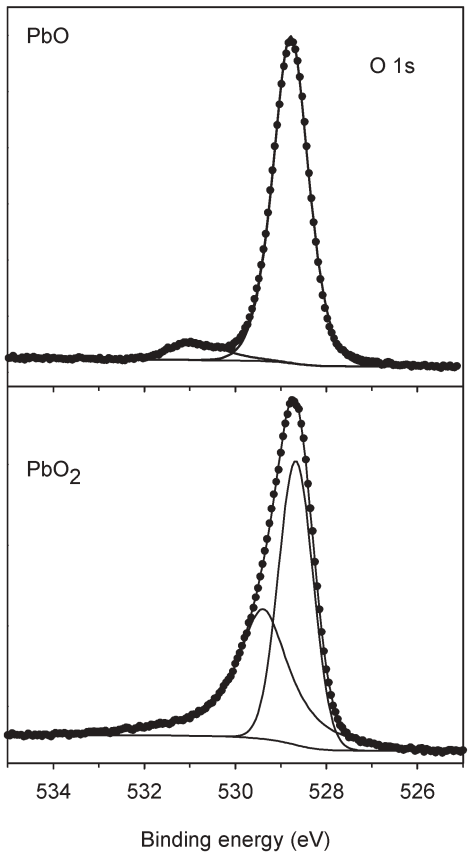

Fig. 10 Al Kα core level photoemission spectra of α-PbO and β-PbO_2 in the O 1s region. See text for discussion of energy referencing.

It was recognized early in the application of photoemission techniques to simple metallic solids that plasmon satellites make a significant contribution to core level structure in X-ray photoelectron spectra. Much of the early work in this area was concerned with unravelling the relative contributions of intrinsic and extrinsic structure and with rationalising the pattern of multiple plasmon excitations.[43] The weak coupling models developed many years ago[44] suggested that the intrinsic plasmon satellite intensity I should increase as the conduction electron density n decreases according to the expression $I \propto n^{-1/3}$. Thus within the framework of this model, the high intensity of the satellites observed in the present work reflects the low density of conduction electrons.

An obvious problem with the plasmon model is that the abnormally *high* satellite intensity calls into question the applicability of a *weak* coupling model in the first place. Moreover, in ''simple'' metals the overall lineshape involves multiple plasmon loss satellites, whereas in the present work only a single satellite is observed. Similar behaviour has been observed in core photoemission of a wide range ''narrow band'' metallic transition metal oxides including the sodium tungsten bronzes Na_xWO_3,[45–53] the superconducting spinel $LiTi_2O_4$,[54,55] dioxides such as MoO_2[55] and RuO_2,[56] and the ternary metallic pyrochlore ruthenates $Pb_2Ru_2O_7$ and $Bi_2Ru_2O_7$.[57] Satellite energies for these materials are all around 1–2 eV. Wertheim and coworkers[45–47] suggested an alternative limiting model for the satellites in this family of narrow band metals. This involves a screening mechanism in which the Coulomb potential of the core hole at an ionised atom creates a localised trap state. In this situation two different final states are then accessible depending on whether the localised state remains empty (giving an unscreened state) or is filled by transfer of an electron from the conduction band (to give a screened final state). In the model developed by Kotani and Toyozawa[58] the screened final state gives rise to an asymmetric line to low binding energy of the lifetime broadened peak associated with the unscreened final state. In the alternative language of the plasmon model the high binding energy unscreened peak corresponds to an extrinsic plasmon satellite whose Lorentzian linewidth will be determined by the conduction electron scattering rate. It still remains a major challenge to reconcile these two different possible descriptions of the satellite structure.

4.5. Effects of *in situ* annealing and sample cooling on spectra of β-PbO_2

The metallic Fermi edge observed in XPS of β-PbO_2 was always found to lie well above the top of the main valence band peak I. However, both the intensity of the Fermi edge cutoff and its position relative to the valence band edge were strongly dependent on the nature of *in situ* treatments, as illustrated in Fig. 11. These observations demonstrate in a simple way that the metallic behaviour arises from variable filling of a conduction band which lies above the main valence

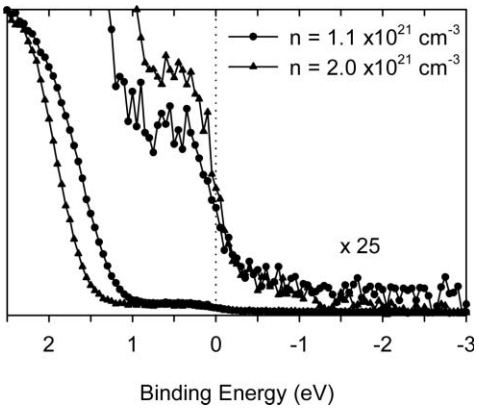

Fig. 11 Al Kα core level photoemission spectra of β-PbO_2 in the region close to the Fermi energy for the two different carrier concentrations indicated. The lower carrier concentration corresponds to an as-presented sample and the higher carrier concentration to a sample annealed to 230 °C for 1 h in UHV.

band. Of course all binding energies are referenced to the Fermi energy and the shifts in the Fermi level within the conduction band are manifest in terms of shifts in the valence band edge to higher binding energy with increasing filling of the conduction band. The downward shift of the valence band edge of 0.26 eV evident in Fig. 11 and the observed increase in the intensity of the Fermi edge as a result of *in situ* annealing at 230 °C may be analysed in terms of the free-electron expressions for the Fermi energy E_F (which defines the position of the Fermi edge observed in photoemission relative to the bottom of the conduction band) and the density of states at the Fermi energy $N(E_F)$:

$$E_F = \frac{\hbar^2}{2m^*}\left(3\pi^2 n\right)^{2/3}$$

$$N(E_F) = \frac{1}{2\pi^2}\left(\frac{2m^*}{\hbar}\right)\left(3\pi^2 n\right)^{1/3}$$

where n is the electron concentration and m^* is the electron effective mass. The measured increase in the density of states at the Fermi energy implies an increase of the conduction electron concentration by a factor of 1.9. Taken in conjunction with the shift in the valence band edge and assuming that $m^* = 0.8m_0$ (where m_0 is the electron rest mass)[3] this variation allows us to deduce that the carrier concentration increases from 1.1×10^{21} cm^{-3} to 2.0×10^{21} cm^{-3} as a consequence of annealing at 230 °C in UHV. The values of the width of the occupied part of the conduction band at the two different carrier concentrations are respectively 0.47 eV and 0.73 eV. This in turn suggests that there is a gap of about 0.7 eV between the top of the valence band and the bottom of the conduction band. That this gap is not immediately evident in XPS could be due to the limited experimental resolution, the effects of secondary electron structure and the possible existence of surface states which fill in the gap region. Note also that in this simple analysis it is not possible to take account of any possible variation in the electron effective mass within the conduction band.

An increase in carrier concentration as a result of annealing at 230 °C in UHV (as determined above from changes in the conduction band structure) may also be inferred from the increase in the energy of the plasmon satellite seen in core XPS. Fig. 12 shows curve fits to the Pb $4f_{7/2}$ core line before and after annealing at 230 °C. The separation between the two components increases from 0.69 eV before annealing to 1.02 eV after annealing. If the satellite is interpreted as a plasmon feature this implies that the carrier concentration increases by a factor $(1.02/0.69)^2 = 2.2$. The increase inferred from conduction band data is by a factor of 1.8, so the agreement between the two techniques is quite reasonable.

We turn finally to consider the effects of cooling thin film samples below room temperature on core level spectra. Fig. 13 shows Pb $4f_{7/2}$ spectra for a sample annealed at 210 °C in UHV for one hour measured at 298 K and 160 K (the lowest temperature achievable in the Scienta spectrometer). From the measured satellite energy of 1.00 eV measured at 298 K (0.02 eV below the value of 1.02 eV found after annealing at 230 °C) we can infer a carrier concentration just below 2×10^{21} cm^{-3}. The satellite energy increases progressively as the temperature decreases, as shown in Fig. 14. Similar changes were found for both higher and lower carrier concentrations.

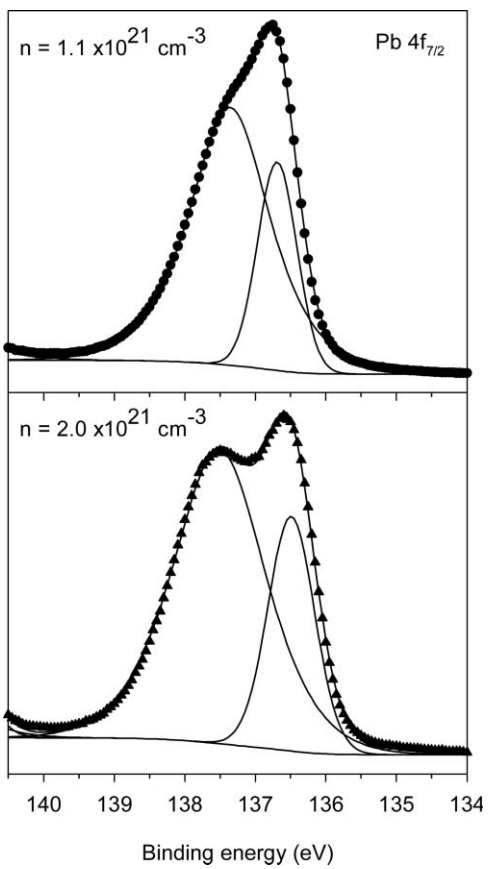

Fig. 12 Pb $4f_{7/2}$ structure in the Al Kα core level photoemission spectra of β-PbO_2 for the two different carrier concentrations indicated. The upper spectrum corresponds to an as-presented sample and the lower spectrum to a sample annealed to 230 °C for 1 h in UHV.

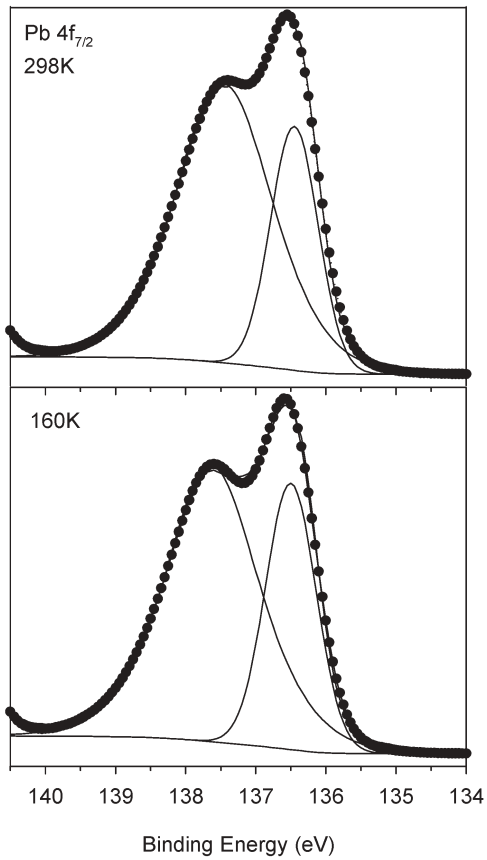

Fig. 13 The Pb $4f_{7/2}$ core line for β-PbO_2 with carrier concentration of 2.0×10^{20} cm^{-3} measured at 298 K and 160 K.

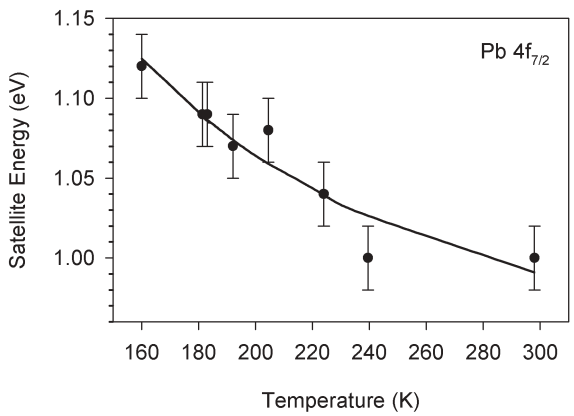

Fig. 14 Temperature dependence of energy of satellite on Pb $4f_{7/2}$ core line.

Small increases in plasmon energies with decreasing temperature have been observed before for simple metals such as Al,[59] Ag[60] and Pb.[61] Here the effect may be linked to thermal expansion with increasing temperature and the corresponding increase in the density of the free electron gas with decreasing temperature. The variations in satellite energy observed in the present work are much too big to be attributable to this mechanism.

The alternative interpretation is that there is a decrease in electron effective mass with decreasing temperature. This in turn could result from narrowing of the bulk bandgap leading to increasing interactions between valence and conduction band states. Although it is usual to find that bandgaps increase with decreasing temperature—and indeed this behaviour is found for the neighbouring oxide SnO_2[62]—for TiO_2 itself the bandgap decreases with decreasing temperature.[63] For PbO_2 we are unaware of any previous investigation of this phenomenon.

5. Concluding remarks

The present work demonstrates that the dominant contribution to the Pb 6s density of states in α-PbO lies about 10 eV below the top of the valence band. A small but significant population of 6s states at the top of the valence band arises due to mixing between O 2p and Pb 6s states to give a lower bonding combination and an antibonding combination at higher energy. Hybridisation between this antibonding combination and nominally empty Pb 6p states is responsible for the structural distortion found in α-PbO. This viewpoint provides a simple explanation of why PbO has a structure where the Pb ions occupy non-centrosymmetric sites but PbS retains a high symmetry rocksalt structure. The anion 3p states in PbS are at higher energy than the anion 2p states of PbO so that the mixing which introduces the metal states to the top of the valence band is less pronounced in PbS and further hybridisation with Pb 6p states is correspondingly suppressed.[12] In SnO and SnS, the cation 5s states are at higher energy than the cation 6s states in PbO and PbS and so in both compounds there is significant mixing between cation 5s and anion *n*p states. Thus both SnO and SnS are subject to structural distortion.[64,65]

The second major conclusion to emerge from the present work is that the Fermi energy in β-PbO_2 lies well above the top of the main valence band. This implies that conduction band states are populated due to donor defects. The fact that the donor concentration may be increased by very gentle annealing in UHV suggests in turn that the donor centres are most likely oxygen vacancy defects. However it is possible that the donors in ''as-presented'' samples are proton interstitials which transform into oxygen defects during the initial stages of annealing according to $H_xPbO_2 \rightarrow PbO_{2-x/2} + x/2H_2O$. Neutron diffraction experiments should be able to distinguish between these two possibilities.

Acknowledgements

We would like to thank the UK EPSRC for support of the NCESS facility. The Boston University program is supported in part by the Department of Energy under DE-FG02-98ER45680. X-Ray emission experiments performed at the Advanced Light Source which is supported by the Director, Office of Science, Office of Basic Energy Sciences, of the U.S. Department of Energy under contract No. DE-AC02-05CH11231. The Trinity College program is supported by the HEA under the cycle III PRTLI award, with the IITAC supercomputing cluster maintained by TCHPC.

References

1 W. Mindt, *J. Electrochem. Soc.*, 1969, **116**, 1076.
2 M. Heinemann, H. J. Terpstra, C. Haas and R. A. de Groot, *Phys. Rev. B*, 1995, **52**, 11740.
3 J. P. Pohl and G. L. Schlechtriemen, *J. Appl. Electrochem.*, 1984, **14**, 521.
4 P. T. Moseley, J. L. Hutchison and M. A. M. Bourke, *J. Electrochem. Soc.*, 1982, **129**, 876.
5 A. F. Wells, *Structural Inorganic Chemistry*, (Clarendon Press, Oxford, 1984).
6 B. B. Van Aken, T. T. M. Palstra, A. Filippetti and N. A. Spaldin, *Nat. Mater.*, 2004, **3**, 164.
7 D. Lebellac, J. M. Kiat, P. Garnier, H. Moudden, P. Sciau, P. A. Buffat and G. Andre, *Phys. Rev. B*, 1995, **52**, 13184.
8 D. M. Adams, *Inorganic Solids*, John Wiley, London, 1974.
9 J. D. Dunitz and L. E. Orgel, *Adv. Inorg. Chem. Radiochem.*, 1960, **2**, 1.
10 G. W. Watson, S. C. Parker and G. Kresse, *Phys. Rev. B*, 1999, **59**, 8481.
11 G. W. Watson and S. C. Parker, *J. Phys. Chem. B*, 1999, **103**, 1258.
12 A. Walsh and G. W. Watson, *J. Solid State Chem.*, 2005, **178**, 1422.
13 A. B. Velichenko, R. Amadelli, A. Benedetti, D. V. Girendko, S. V. Kovalyov and F. I. Danilov, *J. Electrochem. Soc.*, 2002, **149**, C445.
14 S. Abaci, K. Pekmez, T. Hokelek and A. Yildiz, *J. Power Sources*, 2000, **88**, 232.
15 J. Nordgren and R. Nyholm, *Nucl. Instrum. Methods Phys. Res., Sect. A*, 1986, **246**, 242.
16 J. Nordgren, G. Bray, S. Cramm, R. Nyholm, J. E. Rubensson and N. Wassdahl, *Rev. Sci. Instrum.*, 1989, **60**, 1690.
17 G. Kresse and J. Hafner, *Phys. Rev. B*, 1994, **49**, 14251.
18 G. Kresse and J. Furthmuller, *Comput. Mater. Sci.*, 1996, **6**, 15.
19 J. P. Perdew, K. Burke and M. Ernzerhof, *Phys. Rev. Lett.*, 1996, **77**, 3865.
20 P. E. Blochl, *Phys. Rev. B*, 1994, **50**, 17953.
21 H. J. Terpstra, R. A. Degroot and C. Haas, *Phys. Rev. B*, 1995, **52**, 11690.
22 F. D. Murnaghan, *Proc. Natl. Acad. Sci. U. S. A.*, 1944, **30**, 244.
23 A. T. Benjelloun, A. Daoudi and H. Charmette, *J. Chem. Phys.*, 2005, **122**, 154304.
24 R. C. Keezer, D. L. Bowman and J. H. Becker, *J. Appl. Phys.*, 1968, **39**, 2062.
25 J. van den Broek, *Philips Res. Rep.*, 1967, **22**, 36.
26 H. J. Terpstra, R. A. de Groot and C. Haas, *Phys. Rev. B*, 1995, **52**, 11690.
27 Y. Dou, R. G. Egdell, D. S. L. Law, N. M. Harrison and B. G. Searle, *J. Phys.: Condens. Matter*, 1998, **10**, 8447.
28 R. Bader, *Atoms in Molecules: A Quantum Theory*, Oxford University Press, New York, 1990).
29 S. Rondon and P. M. A. Sherwood, *Surf. Sci. Spectra*, 1998, **5**, 97.
30 S. Rondon and P. M. A. Sherwood, *Surf. Sci. Spectra*, 1998, **5**, 104.
31 J. M. Thomas and M. J. Tricker, *J. Chem. Soc., Faraday Trans. 2*, 1974, **71**, 329.
32 U. Gelius, in *Electron Spectroscopy*, ed. D. A. Shirley, North Holland, Amsterdam, 1972, p. 311.
33 J. J. Yeh and I. Lindau, *At. Data Nucl. Data Tables*, 1985, **32**, 1.
34 J. H. Scofield, Lawrence Livermore National Laboratory Report UCRL-51326, 1973.
35 P. A. Glans, T. Learmonth, C. McGuinness, K. E. Smith, J. H. Guo, A. Walsh, G. W. Watson and R. G. Egdell, *Chem. Phys. Lett.*, 2004, **399**, 98.
36 P. A. Glans, T. Learmonth, K. E. Smith, J. Guo, A. Walsh, G. W. Watson, F. Terzi and R. G. Egdell, *Phys. Rev. B*, 2005, **71**, 235109.
37 A. Walsh, G. W. Watson, D. J. Payne, R. G. Egdell, J. Guo, P. A. Glans, T. Learmonth and K. E. Smith, *Phys. Rev. B*, 2006, **73**, 235104.
38 D. J. Payne, R. G. Egdell, A. Walsh, G. W. Watson, J. Guo, P. A. Glans, T. Learmonth and K. E. Smith, *Phys. Rev. Lett.*, 2006, **96**, 157403.
39 R. G. Egdell, J. Rebane, T. J. Walker and D. S. L. Law, *Phys. Rev. B*, 1999, **59**, 1792.
40 R. G. Egdell, T. J. Walker and G. Beamson, *J. Electron Spectrosc. Relat. Phenom.*, 2003, **128**, 59.
41 V. Christou, M. Etchells, O. Renault, P. J. Dobson, O. V. Salata, G. Beamson and R. G. Egdell, *J. Appl. Phys.*, 2000, **88**, 5180.
42 D. J. Payne, R. G. Egdell, W. Hao, J. S. Foord, A. Walsh and G. W. Watson, *Chem. Phys. Lett.*, 2005, **411**, 181.
43 P. Steiner, H. Hochst and S. Hufner, in *Photoemission in Solids II*, ed. L. Ley and M. Cardona, Springer-Verlag, Berlin, 1979.
44 D. C. Langreth, *Nobel Symp.*, 1973, **24**, 210.
45 M. Campagna, G. K. Wertheim, H. R. Shanks, F. Zumsteg and E. Banks, *Phys. Rev. Lett.*, 1975, **34**, 738.
46 J. N. Chazalviel, M. Campagna, G. K. Wertheim and H. R. Shanks, *Phys. Rev. B*, 1977, **16**, 697.
47 G. K. Wertheim, *Chem. Phys. Lett.*, 1979, **65**, 377.
48 R. G. Egdell, H. Innes and M. D. Hill, *Surf. Sci.*, 1985, **149**, 33.
49 G. Hollinger, F. J. Himpsel, N. Mårtensson and B. Reihl, *Phys. Rev. B*, 1983, **27**, 6370.
50 G. Hollinger and P. Pertosa, *Phys. Rev. B*, 1985, **32**, 1987.
51 H. Chermette, G. Hollinger and P. Pertosa, *Chem. Phys. Lett.*, 1982, **86**, 170.
52 G. Hollinger and P. Pertosa, *Chem. Phys. Lett.*, 1980, **74**, 341.
53 G. Hollinger, F. J. Himpsel, B. Reihl, P. Pertosa and J. P. Doumerc, *Solid State Commun.*, 1982, **44**, 1221.
54 P. P. Edwards, R. G. Egdell, I. Fragala, J. B. Goodenough, M. R. Harrison, A. F. Orchard and E. G. Scott, *J. Solid State Chem.*, 1984, **54**, 127.
55 N. Beatham, P. A. Cox, R. G. Egdell and A. F. Orchard, *Chem. Phys. Lett.*, 1980, **69**, 479.
56 P. A. Cox, J. B. Goodenough, P. J. Tavener, D. Telles and R. G. Egdell, *J. Solid State Chem.*, 1986, **62**, 360.
57 P. A. Cox, R. G. Egdell, J. B. Goodenough, A. Hamnett and C. C. Naish, *J. Phys. C: Solid State Phys.*, 1983, **16**, 6221.
58 A. Kotani and Y. Toyozawa, *J. Phys. Soc. Jpn.*, 1974, **37**, 912.
59 G. Meyer, *Z. Phys.*, 1957, **148**, 61.
60 M. Rocca, F. Moresco and U. Valbusa, *Phys. Rev. B*, 1992, **45**, 1399.
61 A. Imbusch and H. Niedrig, *Phys. Lett. A*, 1970, **32**, 375.
62 *Semiconductors: Physics of Non-Tetrahedrally Bonded Binary Compounds II*, ed. O. Madelung, Landolt-Börnstein, New Series, Group III, vol. 17, part f, Springer Verlag, Berlin, 1984.
63 *Semiconductors: Physics of Non-Tetrahedrally Bonded Binary Compounds II*, ed. O. Madelung, Landolt-Börnstein, New Series, Group III, vol. 17, part g, Springer-Verlag, Berlin, 1984.
64 A. Walsh and G. W. Watson, *Phys. Rev. B*, 2004, **70**, 235114.
65 A. Walsh and G. W. Watson, *J. Phys. Chem. B*, 2005, **109**, 18868.